

## Cavitation Instabilities in Inducers

**Yoshinobu Tsujimoto**

Engineering Science, Osaka University  
1-3 Machikaneyama, Toyonaka  
Osaka, 560-8531  
JAPAN

[tujimoto@me.es.osaka-u.ac.jp](mailto:tujimoto@me.es.osaka-u.ac.jp)

### ABSTRACT

*Experimental observations of various kinds of cavitation instabilities are presented. Typical cavitation instabilities occur in the range of cavitation number where the inducer head is not affected by cavitation. This type of cavitation instability is caused by the cavity volume increase due to the increase of incidence angle and is treated in section 1. Another type of cavitation instability is caused by the positive slope of the pressure performance curve due to the blockage effect of cavitation. This type of cavitation instability is treated in section 2. Stability analyses of 1- and 2-dimensional cavitating flow predict various modes of cavitation instabilities. Usually only cavitation surge and forward rotating cavitation are observed. Other modes of cavitation instabilities such as backward rotating cavitation, higher order modes of cavitation surge and rotating cavitation are observed only under limited conditions. Those modes of cavitation instabilities are presented in section 3.*

## 1.0 TYPICAL CAVITATION INSTABILITIES IN A 3-BLADED INDUCER

### 1.1 Experimental Apparatus

The pump loop used is shown in Fig.1 [1]. The baseline experiments were made with an inlet pipe A with an inner diameter 200mm and without the outlet accumulator B. The system parameter was changed by replacing the inlet pipe A with one with a diameter 150mm or by adding an accumulator B with a volume of  $1.5 \times 10^{-3} \text{ m}^3$  under the test condition. The base pressure (and hence the cavitation number) was adjusted by using a vacuum pump connected to the pressure control tank with about  $0.65 \text{ m}^3$  of gas/vapor.

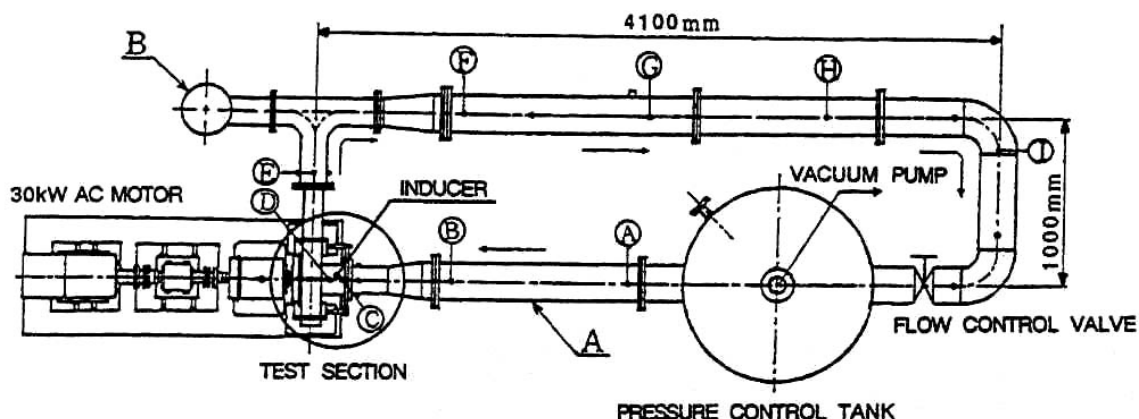


Figure 1: Test Loop.

Tsujimoto, Y. (2006) Cavitation Instabilities in Inducers. In *Design and Analysis of High Speed Pumps* (pp. 8-1 – 8-26). Educational Notes RTO-EN-AVT-143, Paper 8. Neuilly-sur-Seine, France: RTO. Available from: <http://www.rto.nato.int/abstracts.asp>.

Report Documentation Page				Form Approved OMB No. 0704-0188	
Public reporting burden for the collection of information is estimated to average 1 hour per response, including the time for reviewing instructions, searching existing data sources, gathering and maintaining the data needed, and completing and reviewing the collection of information. Send comments regarding this burden estimate or any other aspect of this collection of information, including suggestions for reducing this burden, to Washington Headquarters Services, Directorate for Information Operations and Reports, 1215 Jefferson Davis Highway, Suite 1204, Arlington VA 22202-4302. Respondents should be aware that notwithstanding any other provision of law, no person shall be subject to a penalty for failing to comply with a collection of information if it does not display a currently valid OMB control number.					
1. REPORT DATE <b>01 NOV 2006</b>		2. REPORT TYPE <b>N/A</b>		3. DATES COVERED <b>-</b>	
4. TITLE AND SUBTITLE <b>Cavitation Instabilities in Inducers</b>				5a. CONTRACT NUMBER	
				5b. GRANT NUMBER	
				5c. PROGRAM ELEMENT NUMBER	
6. AUTHOR(S)				5d. PROJECT NUMBER	
				5e. TASK NUMBER	
				5f. WORK UNIT NUMBER	
7. PERFORMING ORGANIZATION NAME(S) AND ADDRESS(ES) <b>Engineering Science, Osaka University 1-3 Machikaneyama, Toyonaka Osaka, 560-8531 JAPAN</b>				8. PERFORMING ORGANIZATION REPORT NUMBER	
9. SPONSORING/MONITORING AGENCY NAME(S) AND ADDRESS(ES)				10. SPONSOR/MONITOR'S ACRONYM(S)	
				11. SPONSOR/MONITOR'S REPORT NUMBER(S)	
12. DISTRIBUTION/AVAILABILITY STATEMENT <b>Approved for public release, distribution unlimited</b>					
13. SUPPLEMENTARY NOTES <b>See also ADM002051., The original document contains color images.</b>					
14. ABSTRACT					
15. SUBJECT TERMS					
16. SECURITY CLASSIFICATION OF:			17. LIMITATION OF ABSTRACT <b>UU</b>	18. NUMBER OF PAGES <b>26</b>	19a. NAME OF RESPONSIBLE PERSON
a. REPORT <b>unclassified</b>	b. ABSTRACT <b>unclassified</b>	c. THIS PAGE <b>unclassified</b>			

Figure 2 shows the test section and the performance curve. The impeller is a scale model of LOX turbopump inducer for HII rocket, with three blades  $Z_i = 3$ , outer diameter 149.8 mm, blade angles at the tip  $7.5^\circ$  at the inlet and  $9.0^\circ$  at the outlet; the housing is made of transparent acrylic resin, with inner diameter 150.8 mm (constant tip clearance of 0.5mm). The inlet pressure fluctuation was measured at 27.5mm upstream of the inducer leading edge, at two circumferential locations with various separation angles  $\theta$ . The number of cells was determined from a plot of the phase difference of those pressure signals. The rotational frequency of the impeller was maintained  $N = 4,000 \pm 2rpm$ . The static pressure performance is also shown in Fig.2. The performance curve has a negative slope throughout the flow range and no conventional surge nor rotating stall is expected to occur. The design point of the inducer is ( $\phi = 0.078$ ,  $\psi_s = 0.130$ ). Since the flow meter was not available at the time of unsteady pressure measurements, the operating condition is shown by using the value of the static pressure coefficient  $\psi_s$ .

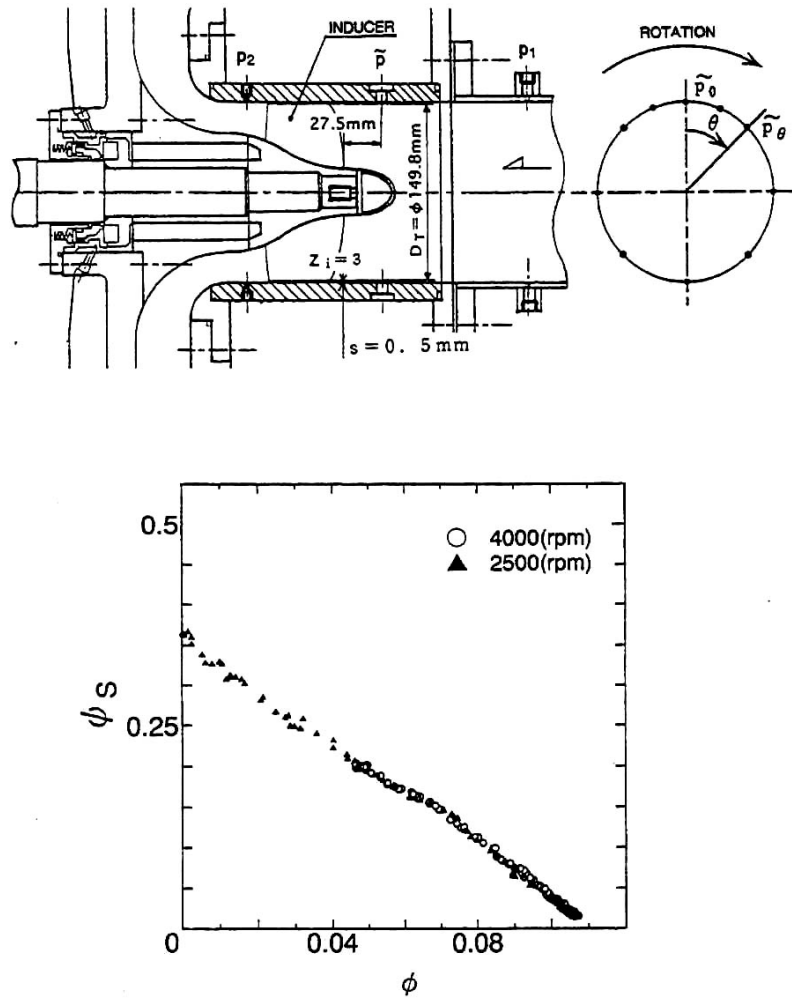


Figure 2: Test Section and Static Pressure Performance.

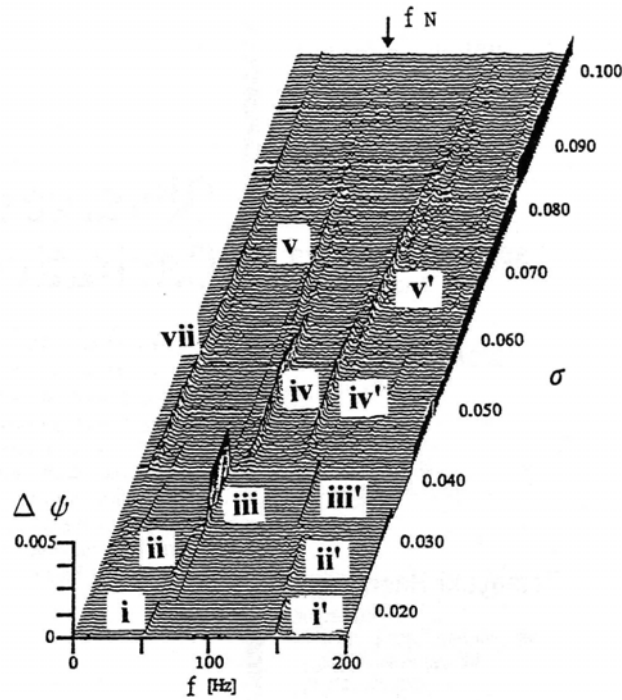
### 1.2 Cell Number Identification

Figure 3(a) shows an example of cascade plot of inlet pressure spectra for various cavitation numbers  $\sigma$ , for a static pressure coefficient  $\psi_s = 0.123$  and a rotational frequency  $f_N = 4000/60 \approx 66.7Hz$ . Hence the blade passing frequency is  $3f_N = 200Hz$ . We observe the frequency components  $i - \nu$  and  $i' - \nu'$ . If we

represent the frequencies of  $i$  and  $i'$  components by  $f_i$  and  $f_{i'}$ , we observe the following relationship

$$f_i + f_{i'} = 3f_N \quad (1)$$

within the accuracy of  $\pm 1.5\text{Hz}$ . Hence, it is quite possible that either one of  $i$  or  $i'$  components is substantial and the other appears as a result of a nonlinear interaction with the blade passing component.



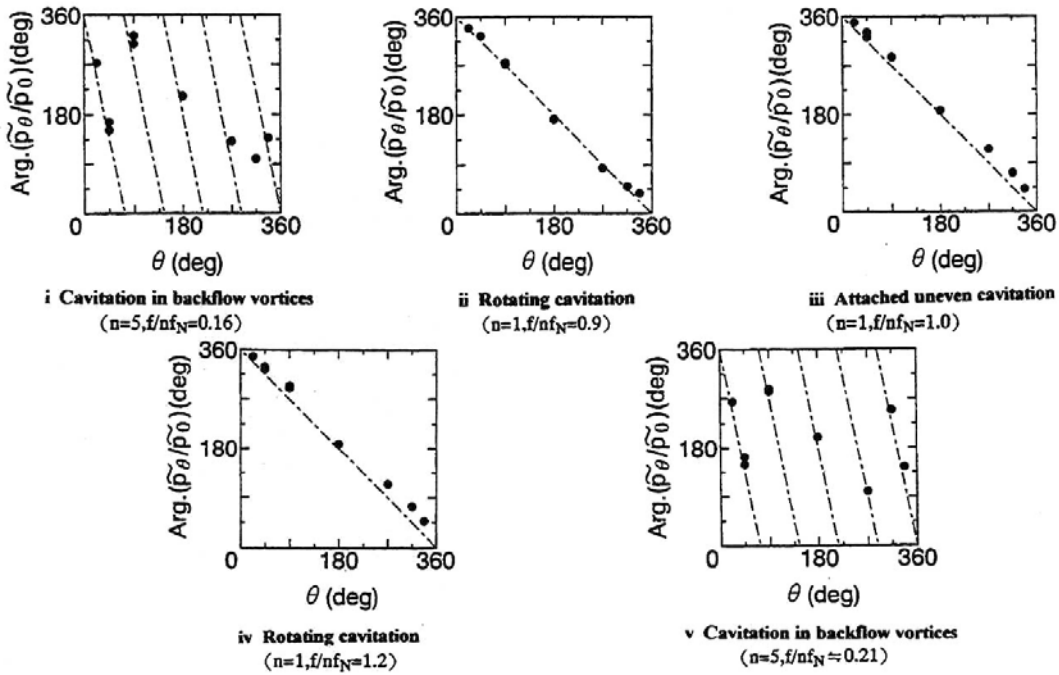
**Figure 3(a): Spectra of Inlet Pressure Fluctuation for  $\psi_s = 0.123 \pm 0.002$ .**

Figure 3(b) shows the phase difference  $\text{Arg}(\tilde{p}_\theta / \tilde{p}_0)$  plotted against the angular separation  $\theta$  of the pressure taps (see Fig.2), where the pressure fluctuation is represented by  $p_\theta = \tilde{p}_\theta \exp(2\pi j f t)$ . By definition, the total amount of the continuous change of  $\text{Arg}(\tilde{p}_\theta / \tilde{p}_0)$  corresponding to the change in  $\theta$  of  $2\pi$ , is  $2\pi$  times the number of cell  $n$ . If  $\text{Arg}(\tilde{p}_\theta / \tilde{p}_0)$  decreases/increases with an increase in  $\theta$ , it shows that the pressure pattern rotates in the direction of/opposite to the impeller rotation. We represent the direction by the plus/minus signs on  $n$  for co-/counter rotating patterns. From the plots similar to Fig.3 (b), the value of  $n'$  for the  $i'$  component is also determined. Then we can obtain the following relationship consistent to the results of nonlinear interaction considerations.

$$n + n' = Z_i = 3 \quad (2)$$

The propagation velocity ratio, defined as the ratio of the rotational velocity of pressure pattern to the impeller rotational frequency is given by

$$f / (n f_N) \quad (3)$$



**Figure 3 (b): Phase Difference  $Arg(\tilde{p}_\theta / \tilde{p}_0)$  Plotted against the Angular Separation  $\theta$  of the Pressure Taps.**

The number of cell  $n$  and the propagation velocity ratio  $f/(nf_N)$  thus determined are shown in Fig.3(b). We cannot distinguish the “substantial” component from the pressure measurements alone. However, from the flow visualization and other studies described later, the components  $i-v$  appear to be the substantial components.

## 1.3 Map of Oscillating Cavitation

Figure 4 presents the cascade plot of inlet pressure power spectra for various values of static pressure coefficient  $\psi_s$ . The design point is  $\psi_s = 0.130$ . The number of cells and the propagation velocity ratio for each component are summarized in Table 1. The ranges of occurrence of each component are shown in the suction performance plots of Fig.5. We should note that all of the instabilities occur in the region of cavitation number where the head is not decreased by cavitation. In addition, they occur both above and below design flow coefficient. These are important characteristics of cavitation instabilities.



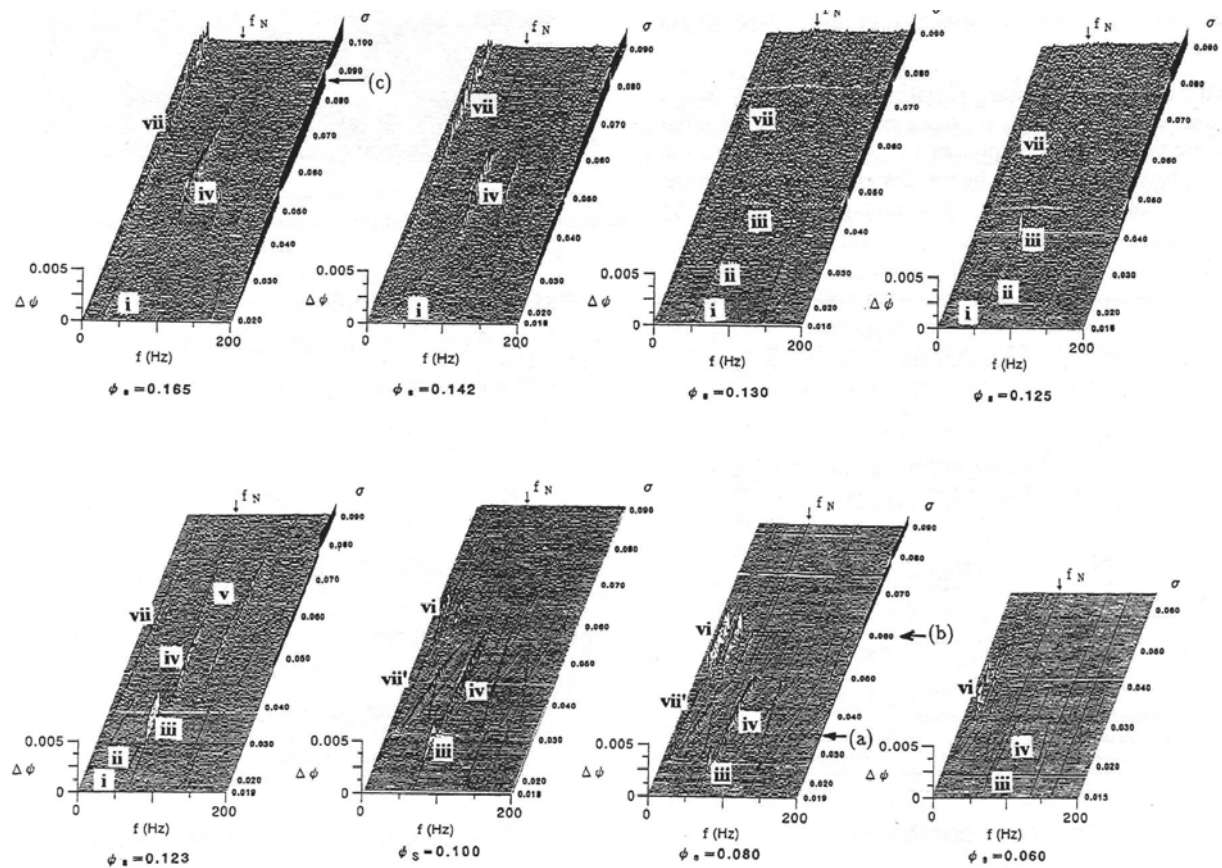


Figure 4: Spectra of Inlet Pressure Fluctuations for Various Static Pressure Rise Coefficient.

Table 1: Number of Cells and Propagation Velocity Ratio

		Number of cells $n$	Rotational velocity ratio $f/nf_N$
<b>i</b>	Cavitation in backflow vortices	5	0.16
<b>ii</b>	Rotating cavitation	1	$\approx 0.9$
<b>iii</b>	Attached uneven cavitation	1	1.0
<b>iv</b>	Rotating cavitation	1	1.1~1.3
<b>v</b>	Cavitation in backflow vortices	5	0.21
<b>vi</b>	Surge mode oscillation	0	$\approx 18\text{Hz} / (3300 \sim 5000 \text{ rpm})$
<b>vii</b>	Cavitation surge	0	8~19Hz/4000 rpm, proportional to rpm

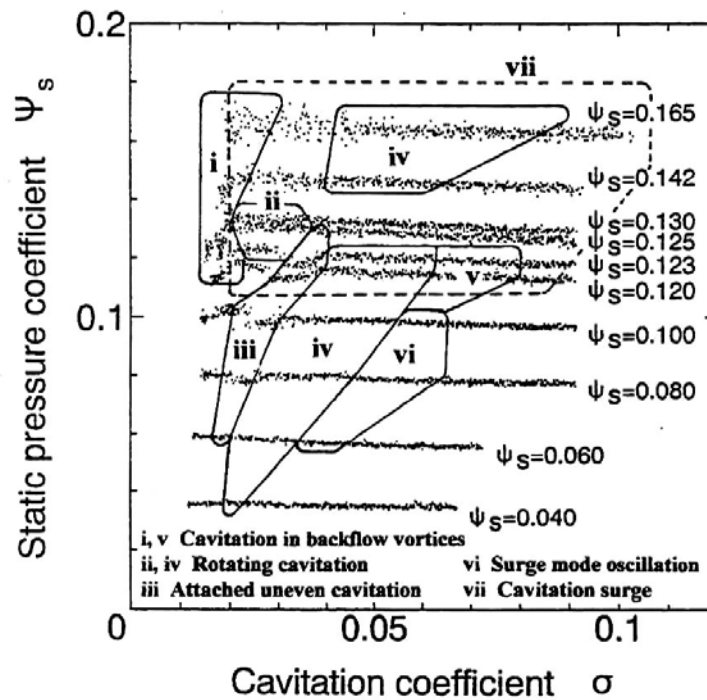


Figure 5: Suction Performance and a Map of Various Oscillating Cavitation Types.

## 1.4 Interpretation of Oscillating Cavitation

### Cavitation in Backflow Vortices.

Figure 6(a) presents a picture from high-speed video under the condition with the component  $i$  at  $\Psi_s = 0.130$  and  $\sigma = 0.015$ . We observe five clouds of cavitation extending upstream from the inducer inlet. They are supposed to be formed in the backflow vortices as observed by Acosta [2]. The cavitation clouds slowly rotate at an angular velocity close to that corresponding to  $f/(nf_N) = 0.16$ . Hence, the component  $i$  is considered to be caused by the backflow vortices. Figure 6(b) shows the picture at a larger cavitation number  $\sigma = 0.07$  where the component  $v$  is found. We find a system of cavitation in the tip leakage flow, which basically rotates attached to the blades, and that in backflow vortices formed on the boundary of the backflow region, rotating much slower than the impeller, as sketched in Fig. 6(c). As shown in Fig 6(b), the backflow vortices occur rather irregularly and it was difficult to determine the its number and speed definitely from the video picture. However, they were found to be consistent with the values  $n = 5$  and  $f/(nf_N) = 0.21$  determined from the pressure measurements. The passage of the backflow vortices is considered to be the cause of the component  $v$ . Although the structure similar to that as sketched in Fig. 6(c) is observed at other conditions, distinct pressure fluctuation could be found only in the regions of  $i$  and  $v$  shown in Fig.5.

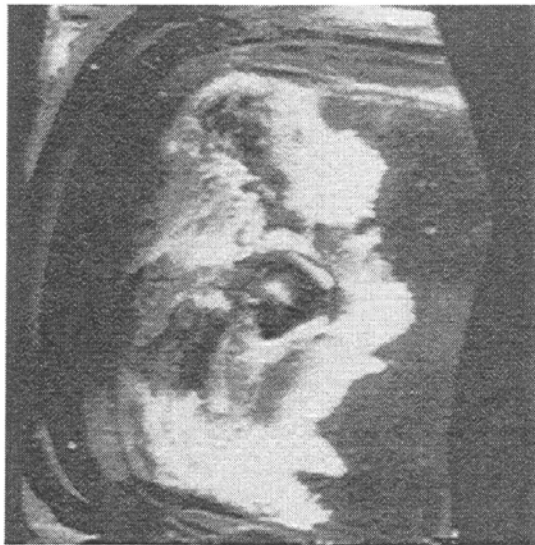


Figure 6(a): Cavitation in Backflow Vortices, Component  $i$ , at Smaller Flow Rate.

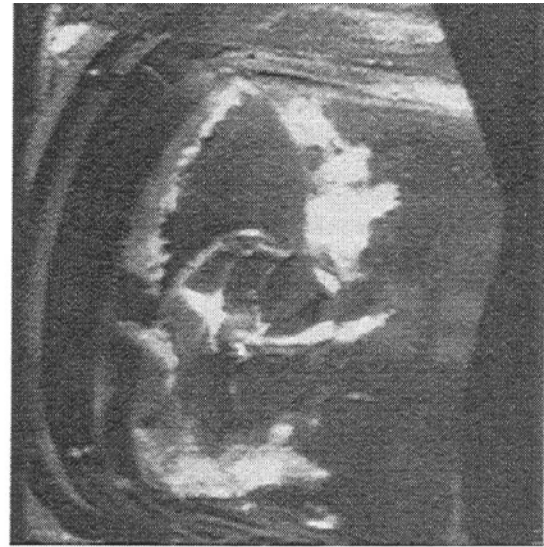


Figure 6(b): Cavitation in Backflow Vortices, Component  $v$ , at Larger Flow Rate.

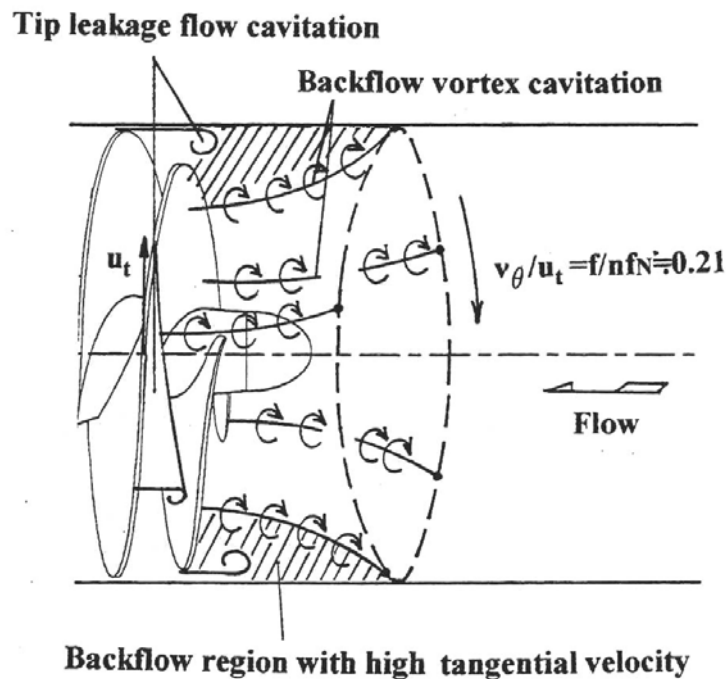


Figure 6(c): Tip Leakage Flow Cavitation and Backflow Vortex Cavitation.

### Forward Travelling Rotating Cavitation.

Figure 7 shows the fluctuation of cavity length  $l_c$  on three blades of the impeller under the condition with the component  $i_v$ . Forward propagation of cavity pattern is clearly shown and hence the component  $i_v$  is the normal rotating cavitation. It should be noted that the maximum cavity length is slightly larger than the circumferential blade spacing  $H$  and the mean value of  $l_c/H$  is about 0.75. As shown in Fig.5, rotating cavitation  $i_v$  appears in two separate regions with  $\psi_s$  larger/smaller than the design value. In the



region with higher static pressure coefficient, the length of blade cavity is smaller and the cavitating region extends more upstream. With the attached cavitation component *iii*, we observe one shorter cavity and two longer cavities fixed to the three blades of the impeller. Hence, the component *iii* is caused by unequal cavities attached to the rotor. With the component *ii*, the change in the size of the cavities is not so clear as with the components *iii* and *iv*. However, the phase plots in Fig.3(b) for *ii* is quite similar to that for *iii* and *iv*. This resemblance suggests that the component *ii* with  $n=1$  and  $f/(nf_N)=0.9$  is substantial. If so, this could be the “backward traveling mode” predicted by the 1-D stability analysis [3]-[5] presented in another lecture of this series.

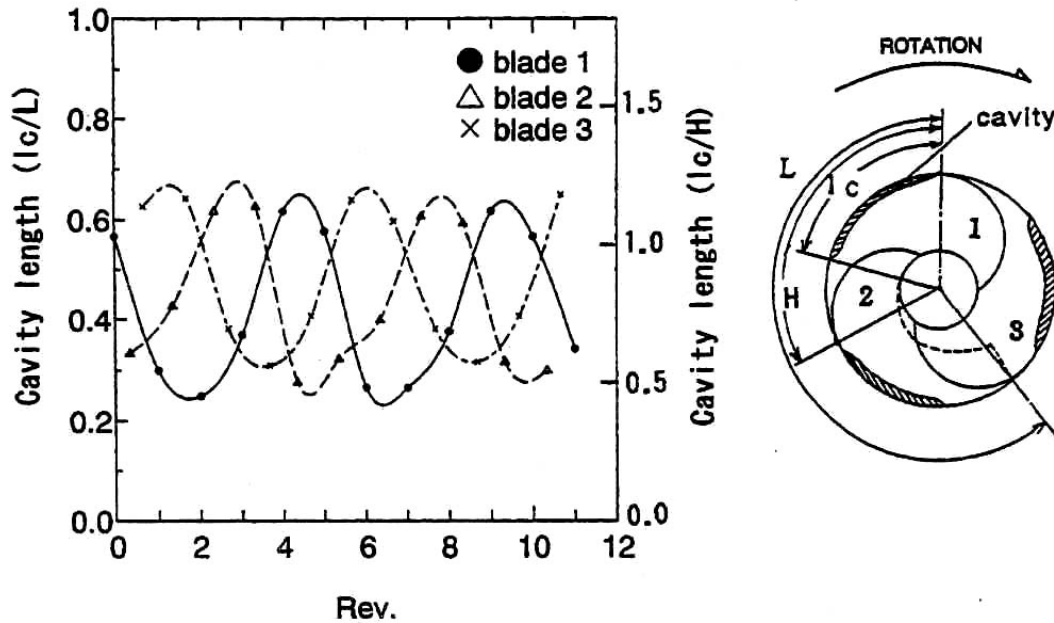


Figure 7: Oscillation of Cavity Length under Rotating Cavitation  
(Component *iv*,  $\psi_s = 0.08$ ,  $\sigma = 0.041$ ).

## Surge Mode Oscillation.

For the components *vi*, *vii*, and *vii'*, the pressure fluctuations are in phase at all circumferential locations. They are called herein “surge mode oscillation” after “surge” in gas handling turbomachines. The fluctuation of the cavity length is plotted in Fig.8 under the surge mode oscillation *vi*. The major differences between the component *vi* and the components *vii* and *vii'* are that, for the component *vi*, the amplitude is larger and the frequency is fairly constant (18 Hz) as shown in Fig.4. Figure 9 shows the effects of rotational frequency  $f_N$  at  $\psi_s = 0.08$ . A detailed examination shows that the frequencies of *iv* and *vii* are proportional to  $f_N$ , while that of *vi* is fixed at 18 Hz. The proportionality of frequency to the rotational speed is an important characteristic of cavitation instabilities. At  $\psi_s = 0.08$ , it was also found that  $f_{iv} - f_N$  is equal to  $f_{vii'}$  within the measurement error ( $\pm 1.5\text{Hz}$ ). Hence, the component *vii'* is caused by a nonlinear interaction of component *iv* (rotating cavitation) with the rotational frequency component. The difference,  $f_{iv} - f_N$ , corresponds to the frequency of cavity oscillation observed on a blade. Figure 9 shows that the component *vi* occurs when the frequency of *vii'* approaches 18 Hz. This suggests that component *vi* is a result of the resonance of a certain vibration mode with 18 Hz and the cavity oscillation due to rotating cavitation. Various attempts have been made to identify the “vibration mode,” but no clear mode could be found.

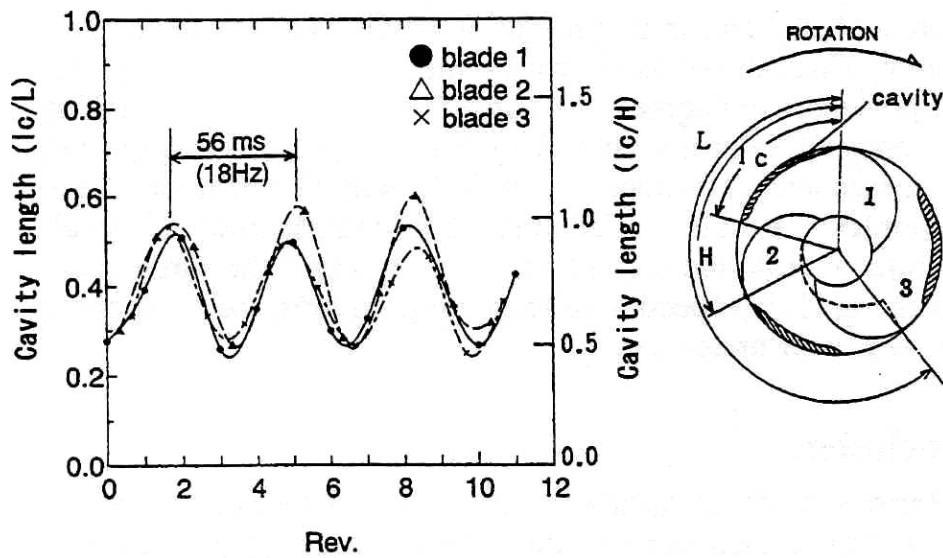


Figure 8: Oscillation of Cavity Length, under Surge Mode Oscillation (Component  $vi$ ,  $\psi_s = 0.08$ ,  $\sigma = 0.054$ ).

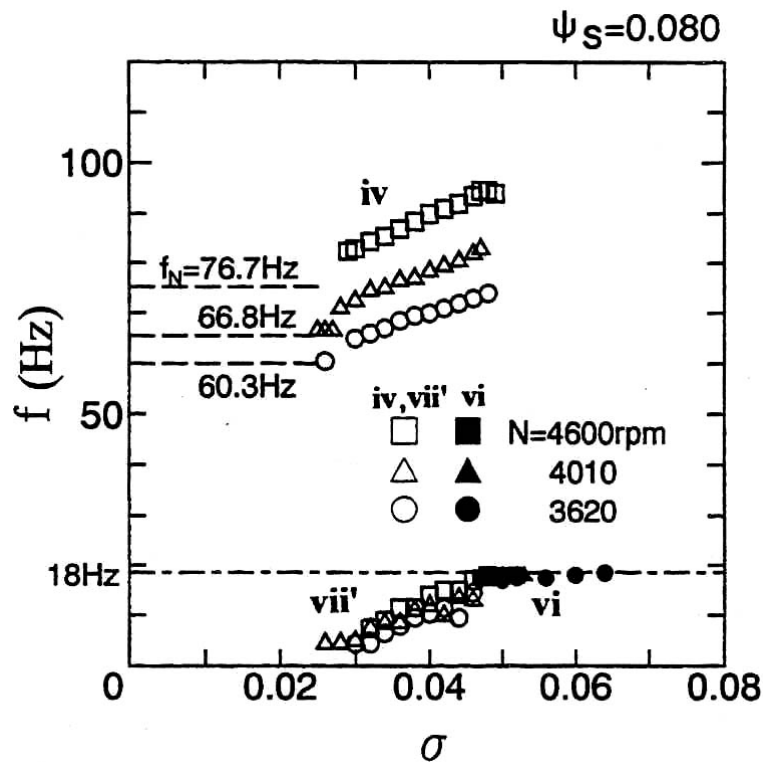


Figure 9: Effects of Rotational Speed  $N$  on the Frequencies of Rotating Cavitation  $iv$ , Surge Mode Oscillation  $vi$ , and Cavitation Surge  $vii'$ .

Although the frequency of  $vii$  is also close to  $f_{iv} - f_N$ , a meaningful difference (larger than  $\pm 1.5\text{Hz}$ , up to  $\pm 5\text{Hz}$ ) was observed. In addition, the component  $vii$  can appear even without the rotating cavitation component  $iv$ . Figure 10 shows the effects of the rotational speed,  $N$ , on the frequency of the component  $vii$ . The frequency is nearly proportional to  $N$  at lower frequencies but the rate of increase decreases at

higher frequencies. The component  $vii$  is considered to be a substantial one and herein called “cavitation surge”, since the proportionality of the frequency to the rotational speed is an important characteristics of cavitation surge. No “resonance” (or, a component equivalent to  $vi$ ) was observed even when  $f_{vii}$  approached 18 Hz. This suggests that the component  $vi$  is not a simple “resonance”.

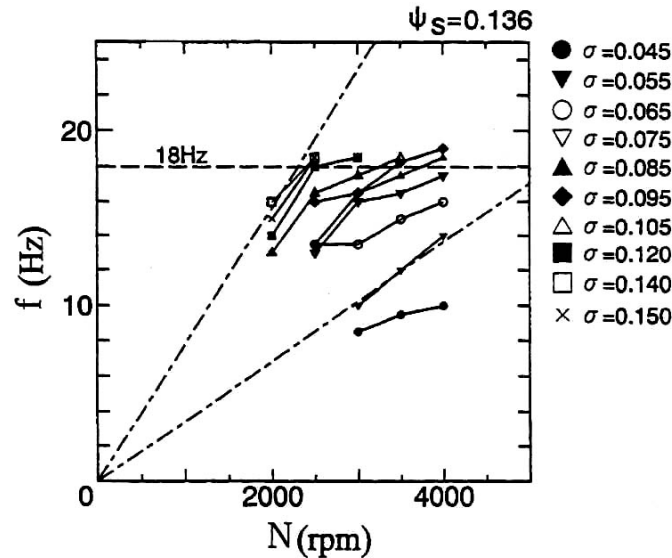


Figure 10: Effects of Rotational Speed  $N$ , on the Frequencies of Cavitation Surge  $vii$ .  
The dash dot lines show proportionality relations between  $N$  and  $f$ .

The modes of pressure fluctuations  $iv$ ,  $vi$ , and  $vii$  in the inlet and outlet pipes are shown in Fig.11. For the surge mode oscillations  $vi$  and  $vii$ , the phase is nearly constant throughout the pipes and the amplitude decreases linearly as the tank is approached from the inducer. The pressure fluctuation amplitude of the rotating cavitation component  $iv$  is significantly smaller at the inducer outlet. It is quite surprising that the rotating cavitation component  $iv$  can be observed as far downstream as 33 impeller diameters from the impeller.

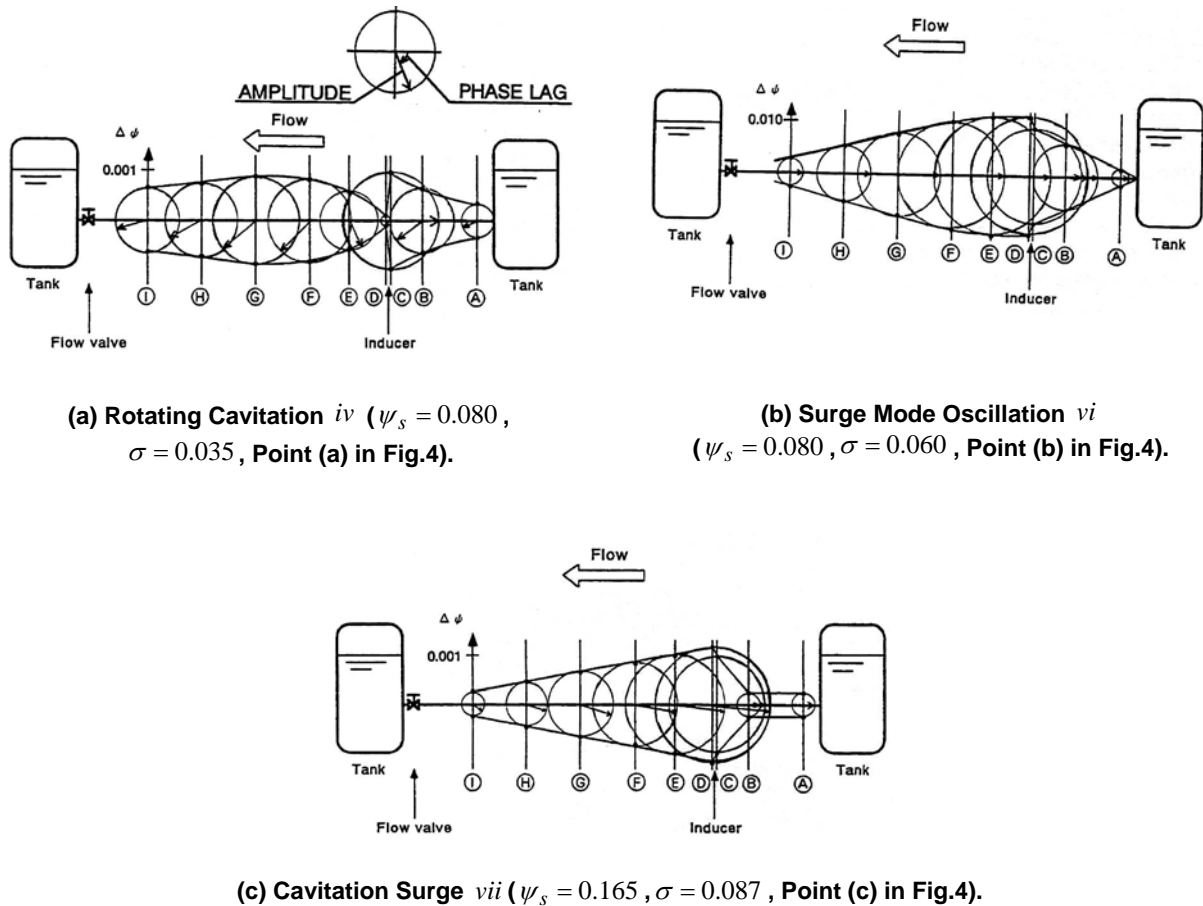


Figure 11: Modes of Pressure Fluctuations  $iv$ ,  $vi$ , and  $vii$  Represented by the Amplitude and the Phase at Each Axial Locations Shown in Fig.1.

## 1.5 Effects of Piping System

In order to examine the effects of piping system, experiments were carried out with the following two additional configurations (see Fig.1):

- Diameter of the inlet pipe A is decreased from 200mm to 150mm (Case I).
- An accumulator B filled with air is added (Case II).

The frequency of each component is plotted in Fig.12. The surge mode oscillation  $vi$  disappeared when we added the accumulator B. We observe no significant change in the frequencies except for the cavitation surge  $vii$ . This shows that all of the rotating cavitation types  $i-v$  are quite independent on the system. The frequency of cavitation surge  $vii$  is decreased by the decrease of the inlet pipe diameter (increase of effective inlet pipe length) and increased by the addition of the tank B (decrease of effective outlet pipe length). Although the frequency of cavitation surge is system dependent as shown above, Brennen [6] proposes an empirical relation between  $f/f_N$  and  $\sigma$  for cavitation surge. This relation is shown by the dashed curve in Fig.12. The present result agrees qualitatively with the empirical relation. The frequency of the surge mode oscillation  $vi$  was not altered by the change of the inlet pipe but it disappeared if we added the accumulator to the outlet line. It disappeared also when a small amount of air was introduced to the outlet line. These observations suggest that the component  $vi$  is closely related with the outlet line but it is not fully understood yet.

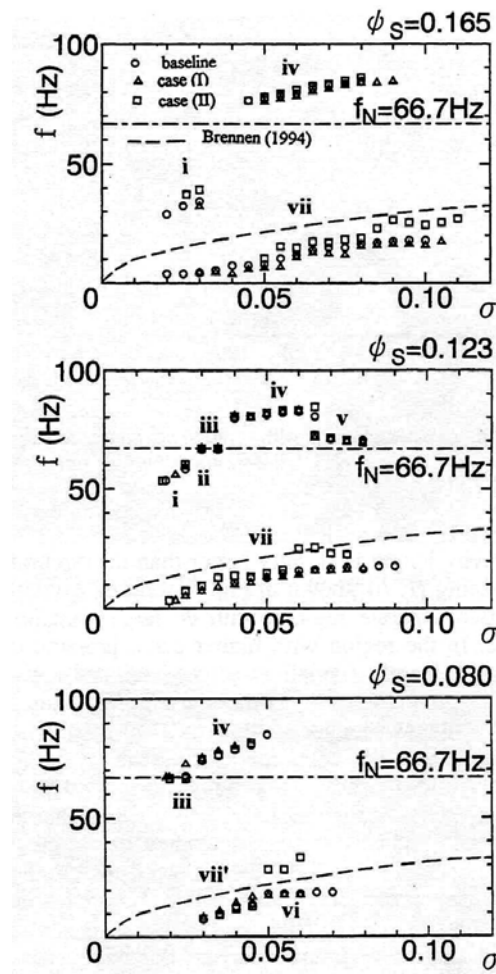


Figure 12: Effect of the Piping System on the Frequencies of Oscillating Cavitation.

## 2.0 CAVITATION INSTABILITY CAUSED BY PERFORMANCE DEGRADATION DUE TO CAVITATION - ROTATING CHOKE

Most of cavitation instabilities occur in a range where the performance degradation due to cavitation is not significant, as shown in the last section. However, in a certain circumstance near head breakdown, another type of cavitation instability caused by the positive slope of the performance can occur. This is treated in this section.

### 2.1 Experimental Observation of Rotating Choke

During the firing test of the LE-7A LOX/LH2 engine of the HIIA rocket, a large amplitude rotor vibration of the fuel turbopump occurred at a frequency of about 350Hz which is about one-half of the shaft rotational speed  $\Omega = 700\text{Hz}$ . The vibration occurred when the pump inlet pressure was reduced. This vibration caused the failure of the bolts fastening the bearing cartridge. To investigate into this phenomenon, a series of tests was conducted at full speed with liquid hydrogen. The test results are reported by Shimura et al.[7].

Figure 13 shows the suction performance and the amplitude of the shaft vibration for two groups of flow rates around  $Q/Q_d = 0.98$  and  $Q/Q_d = 0.95$ . For  $Q/Q_d = 0.95$ , the amplitude becomes larger at the cavitation number where the inducer head decreases rapidly. The head is kept nearly constant, above and



below the cavitation number. The head decrease is not caused by the instability since the head decrease is not recovered at smaller cavitation number where the amplitude of vibration is smaller again. At a cavitation number higher than the breakdown cavitation number,  $\sigma_{high}$ , the head is larger for smaller flow rate and the performance curve has a negative slope in the flow rate vs. head plane. On the other hand, at a lower cavitation number than the breakdown,  $\sigma_{low}$ , the head is smaller for smaller flow rate and the performance curve has a positive slope. These relations are sketched in Fig.14. For compressors and fans, it is well known that the positive slope of the performance curve can cause surge and rotating stall at a smaller flow rate.

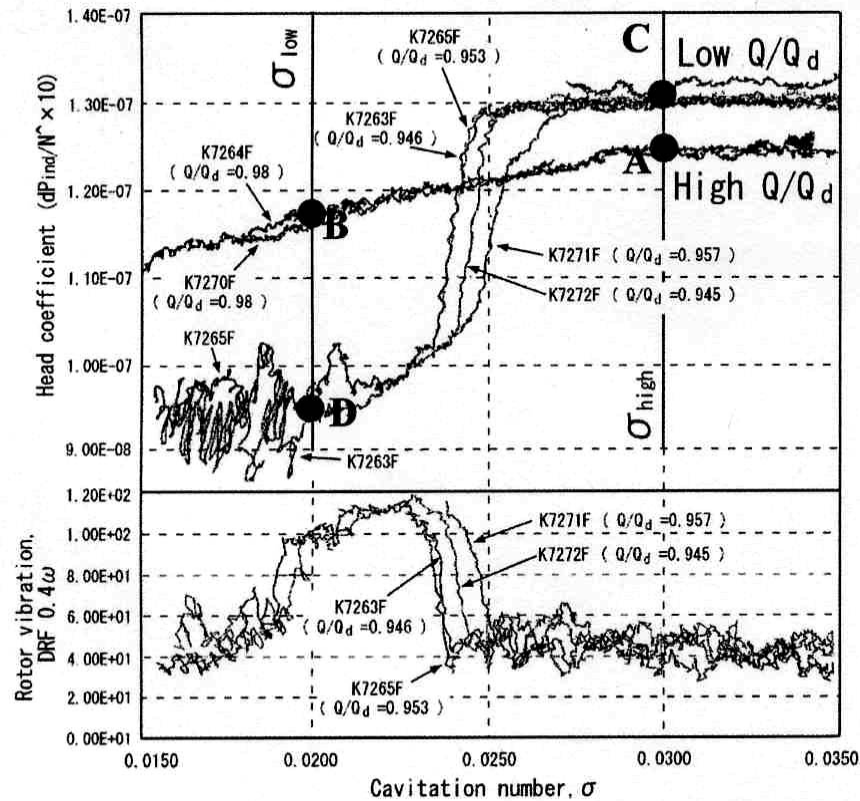


Figure 13: Suction Performance and Shaft Vibration with Two Groups of Flow Rate.

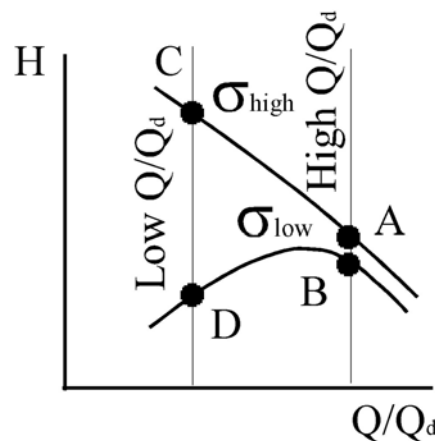


Figure 14: Sketch of Head-Flow Rate Curve.

## Cavitation Instabilities in Inducers

Without cavitation, inducers with smaller blade angle from tangent never stall and the performance curve has positive slope for all flow rate. At higher cavitation number  $\sigma_{high}$  where the cavity does not extend into the flow passage, no head decrease occurs. The head starts to decrease when the cavity extends into the flow channel between blades. It was shown by Stripling and Acosta [8] that the head decrease due to cavitation can be explained by the mixing loss downstream of the cavity terminus. This is called “choke (by cavitation)”. The cavity thickness is larger for smaller flow rate and hence the head decrease due to cavitation is larger, as sketched in Fig.15. If the head decrease due to cavitation associated with the reduction of flow rate is larger than the increase of Euler’s head, the performance curve will have a positive slope. So, it is quite possible that the positive slope at smaller cavitation number is caused by the choke.

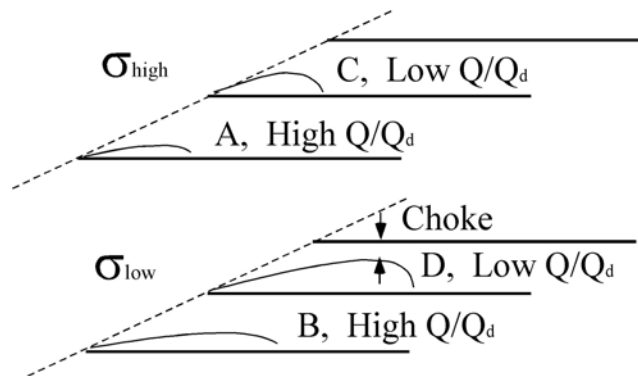


Figure 15: Sketch of Cavity Shape at Higher and Lower Cavitation Number.

Figure 16 shows the spectrum of the inlet pressure fluctuation and the phase difference of the signals from two pressure transducers located apart by 144 degrees circumferentially (Shimura, et al., [7]). The rotational frequency of the impeller is 723Hz. The phase difference at the spectrum peak, 366Hz, is 147 degrees, which is close to the geometrical separation of 144 degrees. This suggests that a disturbance with one cell is rotating around the rotor at 366Hz, with the rotational speed ratio  $366/723=0.506$ . Since the head decrease due to cavitation is caused by choke, it is appropriate to call the instability “rotating choke”. All reported cavitation instabilities occur in a range of cavitation number where degradation of performance due to cavitation is limited. So, this is a new type of cavitation instability caused by the positive slope of pressure performance due to cavitation choke. We should note here that the positive slope of suction performance has a stabilizing effect, as shown by Young et al. [9] for surge mode oscillation.

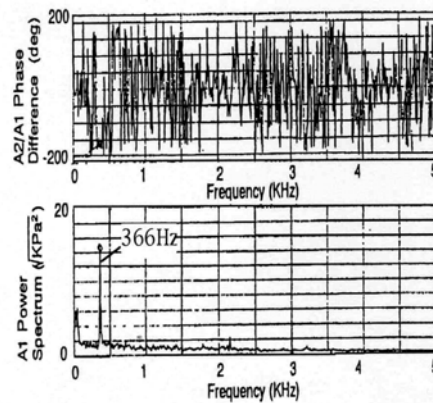


Figure 16: Spectrum of Inlet Pressure Fluctuation and the Phase Difference between Two Pressure Sensors.

## 2.2 Theoretical Analysis of Rotating Choke

Since the instability is associated with the head breakdown due to cavitation, the analytical model should be able to simulate the head breakdown. The closed cavity model cannot predict the head decrease due to cavitation and the results of stability analysis shown in Figure 9 of the companion lecture [5] does not include such instabilities associated with choke. To simulate rotating choke, a cavity model with a cavity wake is applied as shown in Fig.17.

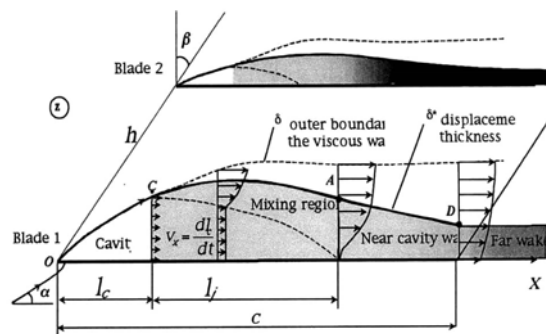
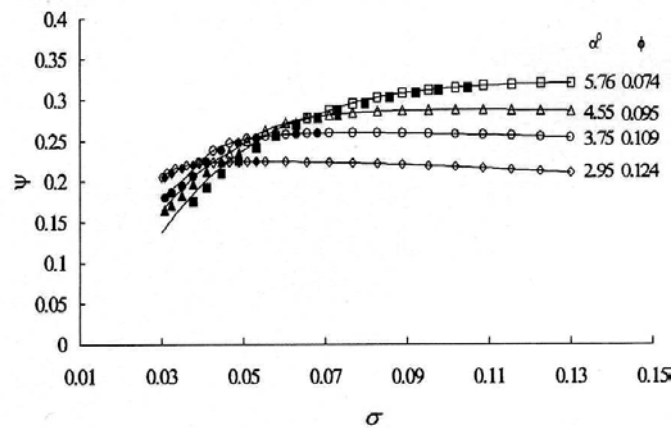


Figure 17: Waked Cavity Model.

The viscous/inviscid interaction approach developed for cavitation-free flows is used. According to this approach the flow is divided into an internal turbulent flow behind the cavity and an external inviscid flow in which the cavity is closed on the body of viscous layer displacement (Semenov et al., [10]). In the cavity wake three specific regions are considered. The first is the transitional mixing region where the velocity profile across the wake is under formation and the density changes smoothly due to flow recirculation. This region is needed to provide a good agreement of suction performance with experiment (Semenov et al., [11]). The second is the near wake in which the velocity profile changes according to the external pressure gradient along the wake. Von Karman's integral equation is used and it is assumed that the coefficient of turbulent mixing is constant (Gogish et al., [12]). The third is the far wake which starts from the trailing edge of blades and adjusts itself on the downstream flow. The conditions of interaction between viscous and inviscid flows in the near wake make it possible to find the shape of the boundary of the inviscid flow and to calculate both steady and unsteady flows. The normal velocity of the outer flow on the boundary is equated with that determined from the change of the wake thickness.

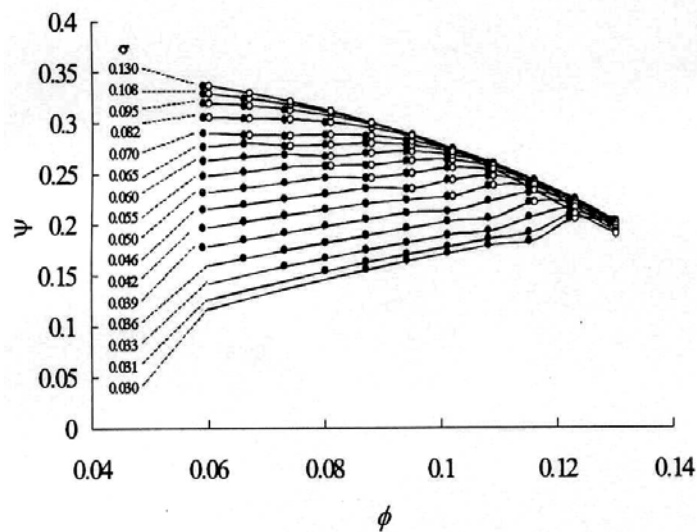
The head decrease due to cavitation is associated with the increase of relative velocity caused by the displacement effect of the cavity wake. The stability analysis is similar to that with closed cavity model (Horiguchi et al., [13],[14]) described in [5]. The problems for the inviscid and viscous flow are reduced to a system of linear equations by using linear interpolation of source and vortex and finite difference approximation of the ordinary differential equations for the viscous wake. The solution of the eigenvalue problem makes it possible to determine the frequencies and the stability of the various modes of cavitation instabilities.

Figure 18 shows the suction performance predicted by the model. On the suction performance curves, the occurrence of rotating cavitation is shown by open symbols, while the occurrence of rotating choke is shown by closed symbols. Other types of instabilities such as shown in Fig.9 of [5] are also predicted by the present model but they are not shown here. We note that the rotating cavitation mainly occurs in the range where the performance degradation is insignificant, while rotating choke occurs where the head is decreased due to cavitation.



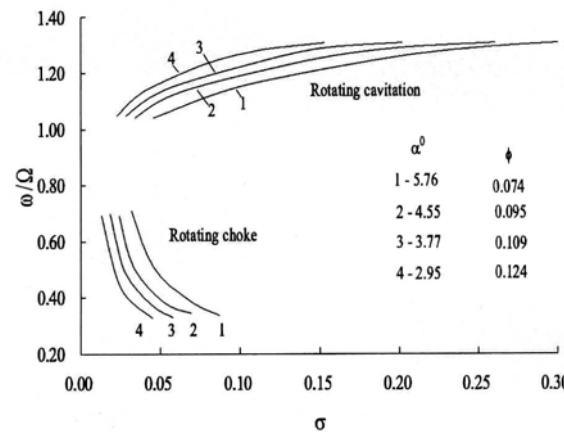
**Figure 18: Suction Performance Predicted by the Waked Cavity Model.**

The performance curve in the flow coefficient vs. head plane is shown in Fig.19, where the occurrences of rotating cavitation and rotating choke are also shown by open and closed symbols, respectively. The same observations as with Fig. 18 are also evident in this figure. Rotating choke occurs typically in the region with positive slope of the performance curve, which is quite different from rotating cavitation. This clearly shows that rotating choke is caused by the positive slope of the performance curve due to choke.



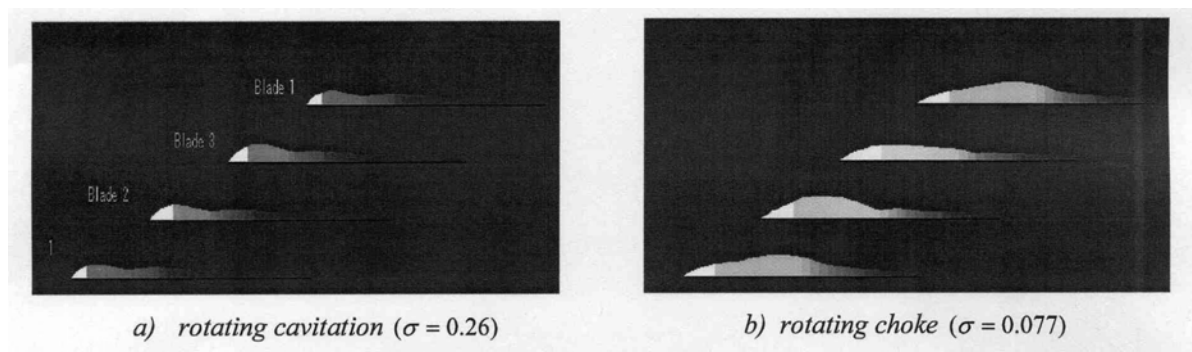
**Figure 19: Head Coefficient-Flow Coefficient Curves for Various Cavitation Number.**

Figure 20 shows the propagation velocity ratio of rotating cavitation and rotating choke. Rotating choke is found only at a region with smaller  $\sigma$ . Rotating cavitation rotates faster than impeller but rotating choke rotates about a half of the impeller speed. Rotating stall in impellers with longer blade rotates with a speed only slightly smaller than the impeller speed, caused by the inertia effect of the fluids in the impeller (Tsujimoto, et al., [3],[4]). Lower speed of the rotating choke may be caused by the decrease of the inertia effect due to cavitation.



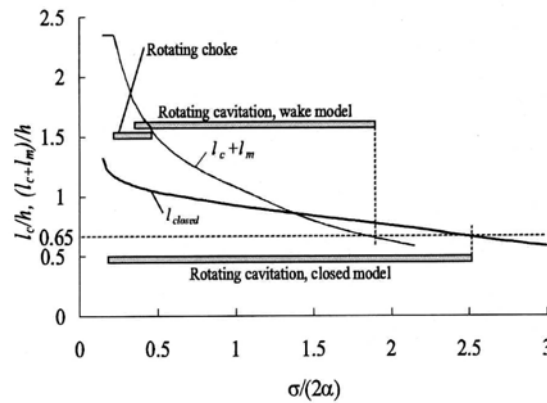
**Figure 20: Propagation Velocity Ratio of Rotating Cavitation and Rotating Choke.**

Figure 21 shows the cavity shapes under rotating cavitation and rotating choke at their onset points (the largest cavitation number). For rotating choke the mixing region extends to the throat of the blade channel. On the other hand, rotating cavitation starts to occur with much shorter cavity. With a closed cavity model, it has been shown that various types of cavitation instability start to occur when the cavity length reaches about 65% of the spacing as mentioned in [5]. Figure 22 shows the steady cavity length  $l_{closed}$  of the closed cavity model and the total length of cavity and mixing region  $l_c + l_m$  of the waked cavity model, normalized by the blade spacing  $h$ , plotted against  $\sigma/(2\alpha)$ . The regions of rotating cavitation and rotating choke occurrence are also shown. It is clearly shown that rotating cavitation starts to occur when the cavity length (closed cavity model) or the total length of cavity and mixing region (waked cavity model) exceeds 65% of the blade spacing,  $h$ . This suggests that the total length of cavity plus mixing region plays an important role in the present model. On the other hand, rotating choke starts to occur when the total length of cavity and mixing region exceeds 150% of the spacing.



**Figure 21: Cavity Shapes at the Onset Point of Rotating Cavitation and Rotating Choke at  $\phi = 0.095$ . Cavity is shown by the white area. The density in the mixing region and the wake is shown by the darkness. Vertical dimension is magnified with a factor 3.**





**Figure 22: Cavity Length of Closed Cavity Model  $l_{closed}$ , and the Total Length of Cavity and Mixing Region  $l_c + l_m$  of the Waked Cavity Model. The gray bars show the range of rotating cavitation and rotating choke. ( $\beta = 80^\circ$ ,  $C/h = 2.35$ ,  $\alpha = 4^\circ$ ).**

Thus, the present model can simulate two important characteristics of rotating choke, the onset condition and frequency. However, predicted suction performance shown in Fig.18 is significantly different from the experimental curve as shown in Fig.13. This may be caused by non-linear and/or three-dimensional effects. Positive slope and hence rotating choke are unusual and not observed for many inducers. Further research is needed for the complete understanding of rotating choke.

## 3.0 HIGHER ORDER MODES OF CAVITATION INSTABILITIES

In addition to cavitation surge and forward mode of rotating cavitation, various kinds of cavitation instabilities are predicted by a 2-dimensional flow stability analysis of a cavitating cascade with a closed cavity model [5]. These modes were subsequently found by experiments and they are treated in this section (Tsujimoto et al., [15]).

### 3.1 Backward Rotating Cavitation

Backward travelling rotating cavitation was identified for the first time by Hashimoto et al. [16]. Figure 23 shows the spectrum of inlet pressure fluctuation of a 3-bladed inducer rotating at  $f_N = 117\text{Hz}$ . Component F with  $f_F = 138\text{Hz}$  is conventional forward propagating rotating cavitation. With this component, an additional component with  $3(f_F - f_N) = 64\text{Hz}$ , which is the frequency at which the blades cut the cavitating region, is observed. At the cavitation number slightly larger than the forward rotating cavitation onset, Component B with  $f_B = 159\text{Hz}$  is observed. With this component, an additional component with  $3(f_B + f_N) = 828\text{Hz}$  is observed. This frequency is obtained if we assume that the cavitated region rotates in the direction opposite to the impeller rotation. Observation of cavity oscillation by high-speed film also suggests backward rotation.

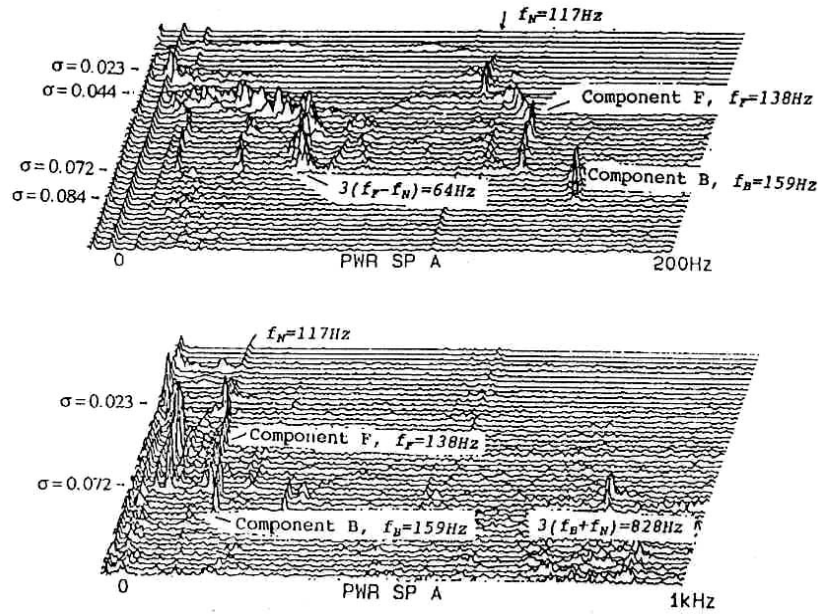
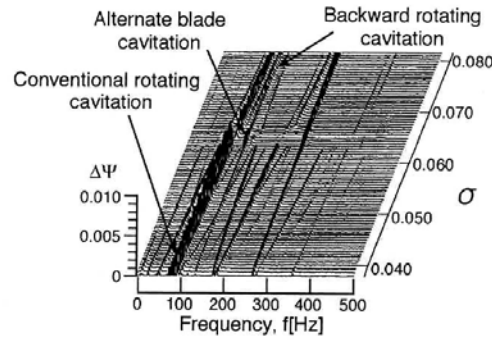
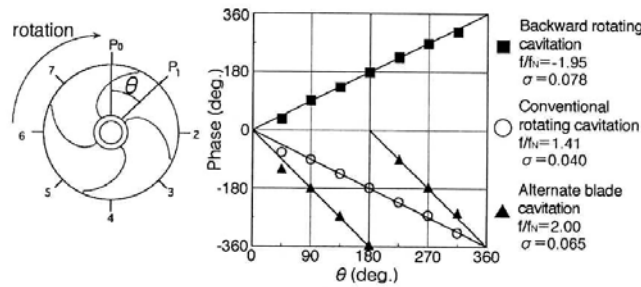


**Figure 23: Spectrum of Inlet Pressure Fluctuation of a 3-Bladed Inducer Showing Forward and Backward Rotating Cavitation.**

Another example of backward rotating cavitation was obtained during the tests of a forward swept 4-bladed inducer. Figure 24 (a) shows the spectrum of inlet pressure fluctuation. The rotational frequency is  $f_N = 66.7\text{Hz}$ . We observe conventional rotating cavitation around  $94\text{Hz}$  ( $f/f_N = 1.41$ ) for the entire range of cavitation number shown. Alternate blade cavitation occurs around  $\sigma = 0.063$ . Backward rotating cavitation is found at  $129\text{Hz}$  ( $f/f_N = (-)1.95$ ) for  $0.065 < \sigma < 0.078$ . This propagation velocity ratio of  $-1.95$  is larger than that for the three bladed inducer ( $-159/117 = -1.36$ ) mentioned before, and is in qualitative agreement with the theoretical results of  $-1.25$  for four bladed inducer and  $-1.0$  for three bladed inducer at  $\sigma/2\alpha = 1.0$ .



(a) Spectrum of inlet pressure fluctuation



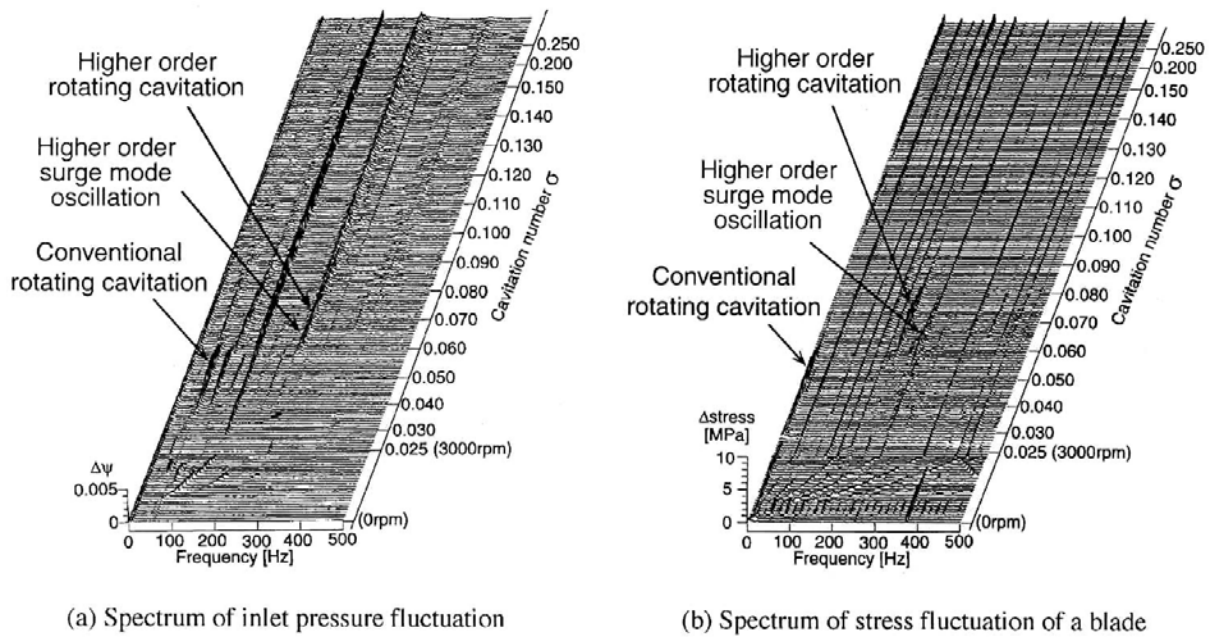
(b) Phase (advance) of pressure fluctuation at various circumferential locations

**Figure 24: Backward Rotating Cavitation Observed in a Forward Swept 4-Bladed Inducer.**

Figure 24 (b) shows the plot of the phase of inlet pressure fluctuation components at various circumferential locations denoted by  $\theta$ . For the backward rotating cavitation, the phase advances as we proceed in the direction of the impeller rotation and reaches 360 degrees as we make one turn. This shows that a pressure pattern with one cell is rotating in the direction opposite to the impeller. Fig. 24(b) also shows that the conventional rotating cavitation and the alternate blade cavitation have one and two cells respectively and that both of them are rotating in the same direction as the impeller.

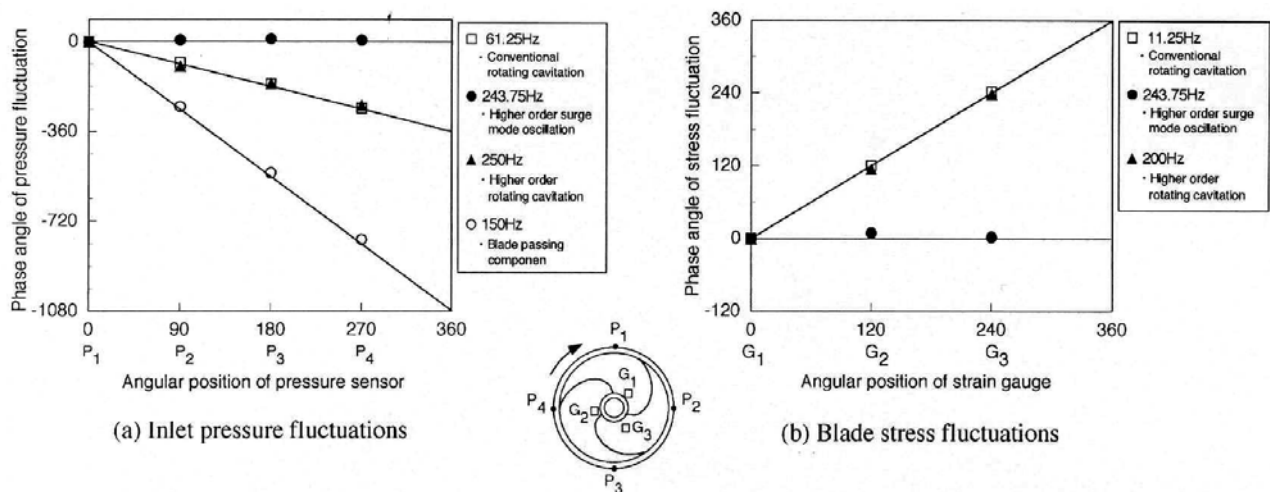
## 3.2 Higher Order Rotating Cavitation

Figure 25 (a) shows the spectrum of the inlet pressure fluctuation observed for a 3-bladed inducer at the rotational speed  $f_N = 50\text{Hz}$ . Conventional rotating cavitation is observed for  $0.04 < \sigma < 0.058$ , at  $f_c = 61.25\text{Hz}$ . In the region of cavitation number larger than that of conventional rotating cavitation onset,  $0.06 < \sigma < 0.09$ , we observe a component with  $f_{h.o} = 250\text{Hz}$ . Although hidden behind the 250Hz component, there is a component with  $f_{hs} = 243.75\text{Hz}$  over  $0.058 < \sigma < 0.068$ . Figure 25(b) shows the spectrum of stress fluctuation of a blade. The components with nearly constant frequency are considered to be electrical noise. With conventional rotating cavitation, for  $0.04 < \sigma < 0.058$ , we observe a component with  $f_c - f_N = 11.25\text{Hz}$  which is the frequency of conventional rotating cavitation observed in the rotating frame. In the same way, we observe a component with  $f_{h.o} - f_N = 200\text{Hz}$ , which is the frequency of forward propagating  $f_{h.o} = 250\text{Hz}$  component observed in the rotating frame. So, this component may correspond to the higher order rotating cavitation. In the region  $0.06 < \sigma < 0.068$ , we observe a component with  $f_{hs} = 243.75\text{Hz}$ , which is the same as that observed in the inlet pressure fluctuation. This can be the higher order surge mode oscillation.



**Figure 25: Spectrum of Inlet Pressure and Blade Stress Fluctuations, Showing a Higher Order Rotating Cavitation and a Higher Order Surge Mode Oscillation.**

Figures 26 (a) and (b) show the phase (positive value means phase advance relative to P1 and G1) of the pressure and stress fluctuations measured at various circumferential locations. They clearly show that both conventional rotating cavitation (with 61.25Hz and 11.25Hz) and the higher order rotating cavitation (with 250Hz and 200Hz) have one cell and rotate in the direction of impeller rotation. The higher order surge mode oscillation with  $f_{hs} = 243.75\text{Hz}$  has the same phase over the circumference. The frequencies of higher order rotating cavitation and higher order surge for 3-bladed inducer predicted by the 2-D stability analysis [5] are both about 4.2 times the rotational frequency at  $\sigma/2\alpha = 1.0$ . This is close to the experimental values of 5.0 and 4.88 for higher order rotating cavitation and higher order surge mode oscillation respectively.



**Figure 26: Phase of Inlet Pressure and Blade Stress Fluctuations, Corresponding to the Spectrum in Fig.25.**

The component in Fig.25 (a) around 240Hz observed over  $\sigma > 0.075$  has low coherence between the pressure signals at different circumferential locations. For this reason, and also because it also occurs at higher inlet pressure without cavitation, we consider that the component is caused by a backflow vortex structure at the inlet.

### **3.3 Higher Order Surge Mode Oscillation**

During the engine firing and water tests for the assessment of the fatigue failure of a blade of the liquid hydrogen turbopump inducer experienced in the 8<sup>th</sup> launch of HII rocket, a high frequency pressure fluctuation was found. The frequency was about 4.7 times the rotational frequency which is close to the first bending mode frequency of the blades. For this reason extensive tests were carried out (Tsujimoto et al., [17]).

Figures 27 (a) and (b) show the spectrum of pressure fluctuations measured at two circumferential locations separated by 90 degrees, on the casing wall and at mid-chord obtained in a water test. The inducer has three blades and the rotational frequency is  $f_N = 150\text{Hz}$ . We observe sharp spectrum peaks at the blade passing frequency  $3f_N$  and its harmonics. In addition, we observe a broadband component centered at 705Hz, which corresponds to 4.7 times the rotational frequency. Note that the peak is higher than the blade passing component. Figure 27 (c) and (d) show the coherence and the phase of the cross spectrum between those pressure signals. We observe high coherence around 705Hz, and the phase difference there is zero. This means that the 705Hz component is a surge mode oscillation. Blade stress fluctuation has similar spectrum and has high coherence with the case pressure fluctuation around 705Hz. This component is important since the frequency can be close to that of the first bending mode of blade vibration.



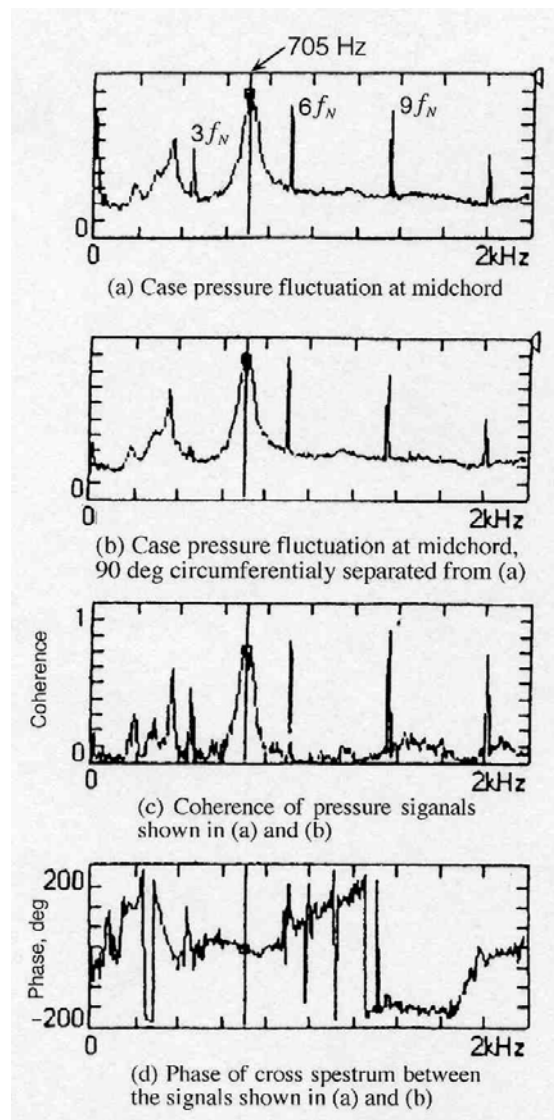


**Figure 27: Spectrum of Pressure Fluctuation at Two Different Circumferential Locations, with Coherence and Phase Difference between the Signals.**

The following characteristics are found in the series of water tests for the 705Hz component:

- (1) The frequency does not depend on the length of inlet pipe. So, it is system independent.
- (2) The onset cavitation number ( $\sigma = 0.1$ ) is significantly larger than that of rotating cavitation ( $\sigma = 0.06$ ).
- (3) The frequency is proportional to the rotational frequency.

The characteristics of (1) to (3) agree with those of the higher order surge mode oscillation (Mode IX) predicted by the 2-D stability analysis in [5].

The Strouhal number of Mode IX based on cavity length is kept nearly constant ( $St = 1.3$ ) and the frequency changes from 3 times the rotational speed at  $\sigma/2\alpha = 0.12$  to 12 times at  $\sigma/2\alpha = 5.61$ . This includes the experimental value, 4.7 times the rotational frequency, but such large dependence on  $\sigma/2\alpha$  was not identified in experiments.

It is unfortunate that further assessment as to closer correlation of the higher order surge mode oscillation with the fatigue failure of the blade. However, it is important to remember that we do have high frequency cavitation instabilities which might resonate with the structural vibration modes of blades.

The backward rotating cavitation, the higher order rotating cavitation, and the higher order surge mode oscillation introduced here are all quite repeatable for each case. However, they can be observed only under limited circumstances, as compared with conventional cavitation surge and rotating cavitation. The reason for that is not known as yet.

## 4.0 CONCLUSION

Experimental observations of various kinds of cavitation instabilities are presented. Typical cavitation instabilities occur in the range of cavitation number where the inducer head is not affected by cavitation. This type of cavitation instability is caused by the cavity volume fluctuation and includes cavitation surge, and forward rotating cavitation. They occur even at design flow coefficient. The frequency of cavitation surge is proportional to the rotor speed and the cavitated region rotates faster than impeller for forward rotating cavitation.

Another type of cavitation instability is caused by the positive slope of the pressure performance curve due to the blockage effect of cavitation. This type of cavitation instability occurs at smaller cavitation number than normal rotating cavitation and the cavitated region rotates slower than impeller.

Stability analyses of 1- and 2-dimensional cavitating flow predict various modes of cavitation instabilities. Usually only cavitation surge and forward rotating cavitation are observed but other modes of cavitation instabilities such as backward rotating cavitation, higher order modes of cavitation surge and rotating cavitation are also observed only under limited conditions. Observed in a frame fixed to the rotor, these higher order modes have very high frequencies and they may excite resonance of blades.

Since cavitation instabilities occur even at design flow rate without head breakdown, they may lead to disastrous results under continuous operation. So, it is important to check that they are adequately suppressed under all operating conditions.

## REFERENCES

- [1] Tsujimoto, Y., Yoshida, Y., Maekawa, Y., Watanabe, S., and Hashimoto, T., (1997). "Observations of Oscillating Cavitation of an Inducer." *ASME Journal of Fluids Engineering*, Vol.119, No.4, December, 775-781.
- [2] Acosta, A.J., (1958). "An Experimental Study of Cavitating Inducers." *Second Symposium on Naval Hydrodynamics, Hydrodynamic Noise, Cavity Flow*. August 25-29, Washington D.C., ACR-38, 533-557.
- [3] Tsujimoto, Y., Kamijio, K. and Yoshida, Y., (1993). "A Theoretical Analysis of Rotating Cavitation in Inducers." *ASME Journal of Fluids Engineering*, Vol.115, No.1, 135-141.
- [4] Tsujimoto, Y., Kamijo, K., and Brennen, C., (2001). "Unified Treatment of Cavitation Instabilities of Turbomachines." *AIAA Journal of Propulsion and Power*, Vol.17, No.3, 636-643.
- [5] Tsujimoto, Y., (2006), "Flow Instabilities in Cavitating and Non-Cavitating Pumps," *RTO-VKI lecture*.
- [6] Brennen, C.E., (1994). *Hydrodynamics of Pumps*. Concepts ETI and Oxford University Press.

- [7] Shimura, T., Yoshida, M., Kamijo, K., Uchiumi, M., Yasutomi, Y., (2002). "Cavitation Induced Vibration Caused by Rotating-stall-type Phenomenon in LH2 Turbopump." *Proceedings of the 9th International Symposium on Transport Phenomena and Dynamics of Rotating Machinery*. Honolulu, Hawaii, February 10-14.
- [8] Stripling, L.B. and Acosta A.,J., (1962). "Cavitation in Turbopump – Part 1." *ASME Journal of Fluids Engineering*, Vol.84, No.3, 326-338.
- [9] Young, W.E. et al., (1972). "Study of Cavitating Inducer Instabilities." *Final Report, NACA-CR-123939*, 1972-8.
- [10] Semenov, Y., Fujii, A., and Tsujimoto, Y., (2004). "Rotating Choke in Cavitating Turbopump Inducer." *ASME Journal of Fluids Engineering*, Vol.126, No.1, 87-93.
- [11] Semenov, Y., and Tsujimoto, Y., (2003). "A Cavity Wake Model Based on the Viscous/Inviscid Interaction Approach and Its Application to Nonsymmetric Cavity Flows in Inducers." *ASME Journal of Fluids Engineering*, Vol.125, No.5, 758-766.
- [12] Gogish, L.V. and Stepanov, G.Yu., (1979). *Turbulent Separated Flows* (in Russian), Moscow, Nauka.
- [13] Horiguchi, H., Watanabe, S., Tsujimoto, Y., and Aoki, M., (2000). "Theoretical analysis of Alternate Blade Cavitation in Inducers." *ASME Journal of Fluids Engineering*, Vol.122, No.1, 156-163.
- [14] Horiguchi, H., Watanabe, S., and Tsujimoto, Y., (2000). "A Linear Stability Analysis of Cavitation in a Finite Blade Count Impeller." *ASME Journal of Fluids Engineering*, Vol.122, No.4, 798-805.
- [15] Tsujimoto, Y., Horiguchi, H., and Fujii, A., (2004). "Non-Standard Cavitation Instabilities in Inducers." *Proceedings of the 10th International Symposium on Heat Transfer and Dynamics of Rotating Machinery*, March 7-11, Honolulu, Hawaii.
- [16] Hashimoto, T., Yoshida, M., Kamijyo, K. and Tsujimoto, Y., (1997). "Experimental Study on Rotating Cavitation of Rocket Propellant Pump Inducers." *AIAA Journal of Propulsion and Power*, Vol.13, No.4, 488-494.
- [17] Tsujimoto, Y., and Semenov, Y., (2002). "New Types of Cavitation Instabilities in Inducers." *Proceedings of the 4th International Symposium on Launcher Technology*, 3-6 December, Liege, Belgium.

